

**UCC Library and UCC researchers have made this item openly available.  
Please [let us know](#) how this has helped you. Thanks!**

<b>Title</b>	Electromagnetic energy harvesting based on HfZrO tunneling junctions
<b>Author(s)</b>	Modreanu, Mircea; Dragoman, Mircea; Povey, Ian M.; Aldrigo, Martino; Dinescu, Adrian; Dragoman, Daniela
<b>Publication date</b>	2018-08-31
<b>Original citation</b>	Dragoman, M. L., Modreanu, M., Povey, I. M., Aldrigo, M., Dinescu, A. and Dragoman, D. (2018) 'Electromagnetic energy harvesting based on HfZrO tunneling junctions', <i>Nanotechnology</i> , 29(44), 445203 (7pp). doi:10.1088/1361-6528/aada6a
<b>Type of publication</b>	Article (peer-reviewed)
<b>Link to publisher's version</b>	<a href="http://dx.doi.org/10.1088/1361-6528/aada6a">http://dx.doi.org/10.1088/1361-6528/aada6a</a> Access to the full text of the published version may require a subscription.
<b>Rights</b>	© 2018, IOP Publishing. All rights reserved. Reproduced by permission of the publisher. This is an author-created, uncopyedited version of an article published in <i>Nanotechnology</i> . IOP Publishing Ltd is not responsible for any errors or omissions in this version of the manuscript or any version derived from it. The Version of Record is available online at <a href="https://doi.org/10.1088/1361-6528/aada6a">10.1088/1361-6528/aada6a</a>
<b>Embargo information</b>	Access to this article is restricted until 12 months after publication by request of the publisher.
<b>Embargo lift date</b>	2019-08-31
<b>Item downloaded from</b>	<a href="http://hdl.handle.net/10468/6732">http://hdl.handle.net/10468/6732</a>

Downloaded on 2021-11-27T05:50:28Z

# ELECTROMAGNETIC ENERGY HARVESTING BASED ON HfZrO TUNNELING JUNCTIONS

Mircea Dragoman<sup>1\*</sup>, Mircea Modreanu<sup>2</sup>, Ian M. Povey<sup>2</sup>, Martino Aldrigo<sup>1</sup>, Adrian Dinescu<sup>1</sup>,  
Daniela Dragoman<sup>3,4</sup>

<sup>1</sup>National Institute for Research and Development in Microtechnologies (IMT Bucharest), Erou  
Iancu Nicolae Street 126A, 077190 Voluntari (Ilfov), Romania,

<sup>2</sup>Tyndall National Institute-University College Cork, Lee Maltings Complex, Dyke Parade, Cork,  
Ireland

<sup>3</sup>Univ. Bucharest, Physics Faculty, P.O. Box MG-11, 077125 Bucharest, Romania

<sup>4</sup>Academy of Romanian Scientists, Splaiul Independentei 54, 050094 Bucharest, Romania

## Abstract

HfZrO ferroelectrics with a thickness of 6 nm were grown directly on Si using atomic layer deposition, top and bottom metallic electrodes being subsequently deposited by electron-beam metallization techniques. Depending on the polarity of the  $\pm 10$  V poling voltages, the current-voltage dependence of these tunneling diodes shows a rectifying behavior for different polarizations, the ON-OFF ratio being about  $10^4$ . Because the currents are at mA level, the HfZrO tunneling diodes coupled to an antenna array can harvest electromagnetic energy at 26 GHz (a bandwidth designated for Internet of Things-IoT), with a responsivity of 63 V/W and a NEP of 4 nW/Hz<sup>0.5</sup>.

---

\*Corresponding author. Email: [mircea.dragoman@imt.ro](mailto:mircea.dragoman@imt.ro)

## 1. Introduction

Ferroelectric HfZrO ( $\text{HfO}_2$  doped with Zr, or  $\text{Hf}_x\text{Zr}_{1-x}\text{O}_2$ ) was discovered a few years ago, when doping  $\text{HfO}_2$  with a range of dopants, including Zr. There is extensive experimental evidence regarding the occurrence of the orthorhombic crystalline structure in HfZrO, which supports ferroelectric behavior [1,2]. Because HfZrO is the first ferroelectric material that is CMOS-compatible at the large wafer scale, many applications have been envisaged in recent years. For instance, in the context of negative capacitance induced by ferroelectrics, HfZrO field-effect transistors (FETs) in a back-gated configuration were shown to reduce the subthreshold swing below 60 mV/decade at room temperature [3] for a device with a channel consisting of flakes of  $\text{MoS}_2$  monolayers, or Si in the case of FinFETs [4]. The negative capacitance is also promising for differential amplification without an external energy source due to polarization switching of the ferroelectric and energy transfer to the dielectric capacitor [5]. On the other hand, microwave applications of HfZrO have emerged, relying on the extraordinary tunability of microwave devices at few volts [6], such as wafer-scale phase shifters based on a 6 nm thick HfZrO ferroelectric grown directly on a high-resistivity silicon substrate, which shows  $60^\circ$  phase shift at 1 GHz when the DC voltage is swept in the range  $\pm 3$  V [7]. Furthermore, an integrated phase antenna array on HfZrO working at 2.55 GHz was developed, formed from two patched antennas, which steer the radiation beam with  $25^\circ$  when the DC voltage is swept within  $\pm 1$  V [8].

Ferroelectric tunneling junctions (FTJ) [9] are in fact metal-insulator-metal (MIM) diodes where the ferroelectric is a few nanometers thick. However, in contrast to MIM diodes (for a review see [10]), the current of FTJs at a certain bias can be switched ON and OFF by the poling voltages, which switch the orientation of ferroelectric domains. On the other hand, these nanodevices are based on very thin ferroelectric layers, in the range of 1-3 nm, and the metallic contact is a problem for tunneling in terms of roughness, so that very often conductive AFM tips replace metallic electrodes. In addition, the ferroelectric materials for FTJs and the substrates on which they are grown, such as:  $\text{BaTiO}_3/\text{La}_{0.67}\text{Sr}_{0.33}\text{MnO}_3$  (BTO/LSMO) [11],  $\text{Sm}_{0.1}\text{Bi}_{0.9}\text{FeO}_3/$

1  
2  
3 Nb:SrTiO<sub>3</sub> (SBFO/NSTO) [12], or Pt/BTO/NSTO [13], are not easily integrable in CMOS  
4  
5 technology. This is a major disadvantage, since CMOS technology is the only one able to  
6  
7 integrate billions of devices on a single chip. In this context, the interest in HfZrO ferroelectric is  
8  
9 very high, not only because it is compatible with CMOS technology, but also thanks to its  
10  
11 physical properties, such as the dependence of permittivity on the applied voltage, hysteretic  
12  
13 current-voltage and/or capacitance-voltage characteristics, and negative capacitance, which are  
14  
15 not currently encountered in integrated CMOS devices.  
16

17  
18         There are many tunneling devices that can be integrated in CMOS technology, but the  
19  
20 MIM configuration is the simplest, MIM devices being the only electronic devices able to work  
21  
22 up to infrared [14]. The ferroelectric MIM (FTJ) allows, in addition, the control of the tunneling  
23  
24 transport, i.e. ON and OFF switching, via DC poling signals. The aim of this paper is thus to  
25  
26 show that even in thicker HfZrO ferroelectric layers (6 nm), which are part of a metal-  
27  
28 ferroelectric-semiconductor (MFS) configuration, the charge transport mechanism is still based  
29  
30 on tunneling, and can be controlled by electric poling signals. This finding can be used for  
31  
32 harvesting the electromagnetic energy at 26 GHz **when HfZrO tunneling diodes are coupled to**  
33  
34 **an antenna array**, in order to feed, for instance, connected devices in an IoT network.  
35  
36  
37  
38

## 39 **2. Fabrication and characterization of tunneling HfZrO devices**

40  
41 We have grown 6-nm-thick Hf<sub>x</sub>Zr<sub>1-x</sub>O<sub>2</sub> layers by atomic layer deposition (ALD), using a  
42  
43 Cambridge NanoTech F200 reactor at 250 °C, on a *p*-doped Si(100) substrate. The following  
44  
45 precursors were involved: Tetrakis(ethylmethyl-amido) hafnium (TEMAHf), Tetrakis(ethyl-  
46  
47 methyl-amido) zirconium (TEMAZr), and water. Both metal precursors have the same nominal  
48  
49 growth rate, of 0.1 nm per cycle, 30 super-cycles of [TEMAHf /H<sub>2</sub>O/TEMAZr/H<sub>2</sub>O] being  
50  
51 employed to generate a well-mixed near 50:50 Hf:Zr composition. Nucleation delays and metal  
52  
53 segregation are assumed to be absent. We have to point out that ALD growth of Hf<sub>0.45</sub>Zr<sub>0.55</sub>O<sub>1.76</sub>  
54  
55 on Si is a very effective method to passivate the Si surface without producing additional defects,  
56  
57  
58  
59  
60

1  
2  
3 thus avoiding the formation of large space-charge regions and surface channels, because of the  
4  
5 formation of a SiO<sub>x</sub> interlayer between HfZrO and Si during growth [15,16].

6  
7 The film thickness, measured by spectroscopic ellipsometry (Woollam M2000), was  
8  
9 found to be 5.8±0.2 nm with the help of a four layer optical model: air/Hf<sub>x</sub>Zr<sub>1-x</sub>O<sub>2</sub>/SiO<sub>2</sub>/Si [17].  
10  
11 The chemical composition of the HfZrO films, namely Hf<sub>0.45</sub>Zr<sub>0.55</sub>O<sub>1.76</sub>, was determined by X-ray  
12  
13 photoelectron spectroscopy (XPS) using a Kratos AXIS ULTRA spectrometer with a source of  
14  
15 monochromatic Al K<sub>α</sub>, of 1486.58 eV. Further details about XPS characterization and grazing  
16  
17 incidence X-ray diffraction patterns, which reveal the ferroelectric, orthorhombic phase with  
18  
19 Pbc21 symmetry of our samples can be found in Ref. 18.

20  
21  
22 To better evidence the ferroelectric behavior of HfZrO thin films, Piezoelectric Force  
23  
24 Microscopy (PFM) experimental data were obtained using the NT-MDT Solver Pro P-47 AFM.  
25  
26 Measurements were performed in piezoresponse force mode by using a low-stiffness conductive  
27  
28 probe (Pt-coated tip with a spring constant of 0.003-0.13 N/m (Tips Nano, CSG01/Pt)). Height  
29  
30 and phase images were acquired by using 256×256 (x,y) positions (pixels). The ferroelectric  
31  
32 property of the Hf<sub>0.45</sub>Zr<sub>0.55</sub>O<sub>1.76</sub> thin film has been assessed by piezoresponse force mode by  
33  
34 applying a bias between the conductive tip and the sample. The images reported in Figs. 1(a) and  
35  
36 1(b) show the surface morphology and the phase, respectively, while a bias was alternated  
37  
38 between +2/-2 V. As already observed by other authors [19,20], the PFM phase image shows a  
39  
40 stripe domains structure induced by an electrically biased scanning tip, while the corresponding  
41  
42 topography, before applying bias, is characterized by a flat structure.

43  
44  
45 In PFM measurements, the ferroelectric behavior is highlighted by the distinct dark and  
46  
47 bright contrast areas that appear as a function of the applied bias. Indeed, during the acquisition  
48  
49 of the images the probe operates by oscillating at a frequency that is close to the characteristic  
50  
51 frequency of the system cantilever-probe-sample, such that the oscillations of the cantilever in  
52  
53 contact with the sample are resonant. Accordingly, the oscillation phase will be different for  
54  
55  
56  
57  
58  
59  
60

1  
2  
3 those domains of the  $\text{Hf}_{0.45}\text{Zr}_{0.55}\text{O}_{1.76}$  film with different orientation of the polarization vector.

4  
5 **For further information on the PFM studies, see [18].**

6  
7 After the  $\text{Hf}_{0.45}\text{Zr}_{0.55}\text{O}_{1.76}$  oxide was grown and characterized, top and bottom electrodes  
8  
9 were deposited using the e-beam evaporation system Temescal FC200. The top electrodes are Cr  
10  
11 (5 nm)/Au (100 nm), with dimensions  $150\ \mu\text{m}\times 150\ \mu\text{m}$ , while the bottom Al electrode has a  
12  
13 thickness of 100 nm. Tens of  $\text{Hf}_{0.45}\text{Zr}_{0.55}\text{O}_{1.76}$  capacitors were fabricated in this manner, Figs.  
14  
15 1(c) and 1(d) presenting an optical image of several of these capacitors (top electrodes) and,  
16  
17 respectively, the schematic cross-section of these devices.  
18  
19

20 The electrical characterization of MFS devices was performed between the top and the  
21  
22 bottom electrode, which plays the role of ground electrode. All measurements were carried out  
23  
24 using a Keithley SCS 4200 station with all channels connected to low noise amplifiers. The  
25  
26 station is connected to a probe station, on which the chip containing all devices is placed. The  
27  
28 entire probe station is enclosed in a Faraday cage. All experiments are performed inside the  
29  
30 Faraday cage, which is closed during measurements. In order to check for hysteretic behavior of  
31  
32 MFS devices, electrical characterizations were performed at various voltage sweeps. No fitting  
33  
34 algorithms were applied during or after measurements. The yield was very good: 95% of the  
35  
36 MFS capacitors showed similar capacitance-voltage (C-V) characteristics, within  $\pm 5\%$   
37  
38 dispersion, while 5% of all devices had problems due to their metallic contacts, which were  
39  
40 exfoliated during the positioning of the sharp metallic probe tips.  
41  
42  
43

44 The typical C-V dependences, displayed in Fig. 2, demonstrate a hysteretic behavior,  
45  
46 which have a counterclockwise trace, caused mainly by the interfacial layer formed during ALD  
47  
48 deposition and located between the ferroelectric and the Si substrate [21,22]. This layer at the  
49  
50 ferroelectric/semiconductor interface consists of residual impurities acting as slow states and  
51  
52 related to hydroxyl groups formed during ALD growth from water. The hysteretic C-V  
53  
54 dependences in Fig. 2 were recorded at 100 kHz, for different sweeping ranges indicated in the  
55  
56 legend. As can be seen from the inset of this figure, the window (the width of the hysteresis  
57  
58  
59  
60

loop) increases initially with the sweeping range and then decreases, due to an increased number of charge carriers that tunnel through the very thin ferroelectric layer at larger applied voltages.

A typical DC current-voltage dependence of the MFS devices, for poling signals of opposite polarity, is shown in Fig. 3(a) and reveals the existence of two distinct conduction states of HfZrO devices, termed ON and OFF. **The corresponding band diagrams of the MFS structures in the absence of an applied bias are represented in Fig. 3(b). As can be seen from this figure, the opposite poling signals, which define the ON and OFF states, cause an opposite orientation of the dipole in the ferroelectric layer, equivalent to a built-in field, which modifies the band diagram of the devices. Thus, the currents/resistances in the ON and OFF states are different, inducing the rectifying behavior.** In order to obtain the current-voltage characteristic depicted in Fig. 3(a), we applied the following procedure: before measurement, a poling signal consisting of a ramp of +10 V was applied to the device for 20 s, and the I-V dependence was measured in the ON state (black line). Then, the same poling signal, with the same duration but reversed polarity (-10 V) was applied on the device, which was measured in the OFF state (red line). The procedure was applied several times for each device to see if the ON and OFF states are preserved, but no significant changes were detected. In order to identify the conduction mechanism in the MFS device, we fitted the experimental data with different formulas, corresponding to different mechanisms, the best fit being obtained for the Fowler-Nordheim tunneling, for which [23]:

$$I \propto E^2 \exp\left(\frac{-4\sqrt{2em}}{3\hbar E} \phi_b^{3/2}\right) \quad (1)$$

where  $E$  is the electric field,  $m$  the effective mass of electrons and  $\phi_b$  the barrier height at the ferroelectric/Si interface. The fit is presented in the top inset of Fig. 3(a), the value of  $\phi_b$  calculated from the slope of the fit (red line), for an electron effective mass in HfZrO of  $0.47m_0$

[24], with  $m_0$  the free electron mass, being about 0.3 V. The identified tunneling mechanism explains also the shape of the C-V curve corresponding to largest sweeping voltage employed, i.e of +/-5 V. More precisely, the decrease of the capacitance at large biases is caused by tunneling, more probable at high voltages, which decreases the charges contributing to the capacitive response.

The ratio of the ON and OFF currents (corresponding to poling signals of opposite polarities) is about  $10^4$ , as can be seen from the bottom inset of Fig. 3(a), which represents the  $\log(I)$ -V characteristics. The two dependences are drawn with the same line type as that used for the corresponding I-V characteristics.

### 3. Fabrication and characterization of an antenna array at 26 GHz and of an $\text{Hf}_{0.45}\text{Zr}_{0.55}\text{O}_{1.76}$ -based energy harvester

Because the currents of the rectifying HfZrO tunneling diodes are at mA level, the diodes can be coupled to an antenna array in order to harvest electromagnetic energy at 26 GHz (a bandwidth designated for Internet of Things-IoT). Therefore, we have also fabricated an antenna array at 26 GHz using optical lithography, measured it, and used its electromagnetic parameters to estimate the performance of the harvester when interconnected with the  $\text{Hf}_{0.45}\text{Zr}_{0.55}\text{O}_{1.76}$  MFS device (see Fig. 4). The antenna array was fabricated on a  $\text{SiO}_2$  substrate (300 nm thick) thermally deposited on 525- $\mu\text{m}$ -thick high-resistivity silicon (HR Si). The metallization is a 500 nm thick gold layer. The width and length of an antenna patch are  $W = 2.22$  mm and  $L = 1.46$  mm, respectively, while the spacing between antennas is about  $\lambda_0/2$  in the  $(x,y)$  directions, with  $\lambda_0$  the free-space wavelength. In our case,  $\lambda_0 \approx 11.54$  mm at 26 GHz. The reference antenna input impedance is 50  $\Omega$ .

We have measured the antenna return loss ( $|S_{11}|$ ) and the imaginary part of its input impedance, the results being shown in Figs. 5(a) and 5(b), respectively. From the first figure it follows that the best matching to 50  $\Omega$  occurs at 25.9 GHz from simulations, while it is found at



1  
2  
3 27.8 GHz from measurements. The difference between simulated and measured  $|S_{11}|$  values is  
4 explained by the large difference between the thickness of the antenna array (of 500  $\mu\text{m}$ ) and the  
5 free space wavelength (about 20 times larger, i.e. 1.15 cm at 26 GHz). Due to this fact, the  
6 antenna array does not radiate only above the radiation plane, represented by the antenna  
7 patches, but also below it, and the radiation efficiency is reduced. Therefore, during  
8 measurements the antenna array was mounted on a metallic support (not considered in  
9 simulations due to the very large computational time needed), to reduce the unwanted reflections  
10 and to increase its radiation efficiency. Nevertheless, the simulated and measured resonances (for  
11 which the imaginary part of the antenna input impedance is equal to zero) are very closely  
12 spaced, i.e. at 25.66 GHz from simulations and 25.14 GHz from measurements.

23  
24 To demonstrate the possibility of using MFS devices coupled to antenna arrays as  
25 electromagnetic energy harvesters, we integrated the MFS device in a coplanar (CPW)  
26 waveguide connected to the antenna array via a CPW taper. The output of the CPW MFS is  
27 further connected, by another CPW taper, to an optimized load  $R = 280 \Omega$  in parallel with  $C = 5$   
28 pF (see Fig. 6). Using the AWR simulator, in which we introduced the experimental  $I$ - $V$  data, we  
29 further estimated the time domain response of the harvester (see Fig. 7) at various microwave  
30 voltages. The responsivity and NEP at various microwave voltages is displayed in Fig. 8. For an  
31 incident power between -20 dBm and 10 dBm, the responsivity is in the 63.34-0.47 V/W range,  
32 whereas the NEP spans the range 3.84-514.46 nW/Hz<sup>0.5</sup>. A comparison of our rectenna (i.e. the  
33 antenna array integrated with the HfZrO diode) with other existing rectennas in terms of the  
34 performance for harvesting millimeter waves working in the same bandwidth is difficult since  
35 the conversion efficiency defined as  $\eta = P_{DC} / P_{RF} [\%]$  is generally calculated at various  
36 frequencies and various load resistances. Here  $P_{DC}$  is the DC power, while  $P_{RF}$  is the input RF  
37 power at a given frequency. However, considering the RF power as 0 dBm (10 mW) we obtain  
38 an efficiency of 6% at 26 GHz, while 10% efficiency is obtained at the same RF power at 24  
39 GHz with a rectifier consisting of a commercial Schottky diode [25].  
40  
41  
42  
43  
44  
45  
46  
47  
48  
49  
50  
51  
52  
53  
54  
55  
56  
57  
58  
59  
60

#### 4. Conclusions

In this paper, HfZrO ferroelectrics with a thickness of 6 nm were grown directly on Si using atomic layer deposition, top and bottom metallic electrodes being subsequently deposited by electron-beam metallization techniques. Depending on the polarity of the  $\pm 10$  V poling voltages, the current-voltage dependence of these HfZrO tunneling diodes shows a rectifying behavior for different polarizations, the ON-OFF ratio being about  $10^4$  and the currents having large values, of mA level. We have demonstrated that, by using a metal-ferroelectric-semiconductor device **coupled to an antenna array**, we can collect electromagnetic energy at 26 GHz, with a responsivity of 63 V/W and a NEP of  $4 \text{ nW/Hz}^{0.5}$ , high enough to feed things with a very low power consumption connected in an IoT network. For example, processors for sensing applications as in IoT consume only 35 pW in the standby mode, and 290 nW in the active mode [26]. Such types of extremely complex low-power circuits can be fed wirelessly by the harvester proposed in this work. In fact, many other things in an IoT besides sensors could be fed in the same way, since the required active power levels are fractions of  $\mu\text{W}$  [27].

#### Acknowledgments:

The authors would like to thank Prof. Marco Farina, Dr. Andreea Di Donato and Dr. Eleonora Pavoni from Università Politecnica delle Marche, Ancona, Italy for performing the Piezoresponse Force Microscopy measurements on our samples.

Some of the authors (MD, MA, AD and DD) acknowledge the financial support of project number PN-III-P4-ID-PCCF-2016-0033.

## References

- [1] D. Martin, J. Müller, T. Schenk, T. M. Arruda, A. Kumar, E. Strelcov, E. Yurchuk, S. Müller, D. Pohl, U. Schröder, S. V. Kalinin, and T. Mikolajick, Ferroelectricity in Si-doped HfO<sub>2</sub> revealed: a binary lead-free ferroelectric, *Adv. Mater.* 26, 8198-8202 (2014).
- [2] Z. Fan, J. Chen, and J. Wang, Ferroelectric HfO<sub>2</sub>-based materials for next generation ferroelectric memories, *J. Advanced Dielectrics* 6, 1630003 (2016).
- [3] M. Si, C.-J. Su, C. Jiang, N. J. Conrad, H. Zhou, K. D. Maize, G. Qiu, C.-T. Wu, A. Shakouri, M. A. Alam, and P. D. Ye, Steep-slope hysteresis-free negative capacitance MoS<sub>2</sub> transistors, *Nature Nanotechnology* 13, 24-28 (2018).
- [4] E. Ko, H. Lee, Y. Goh, S. Jeon, and C. Shin, Sub-60-mV/decade negative capacitance FinFET with sub-10-nm hafnium-based ferroelectric capacitor, *IEEE J. Electron Devices Society* 5, 306-309 (2017).
- [5] A. I. Khan, M. Hoffmann, K. Chatterjee, Z. Lu, R. Xu, C. Serrao, S. Smith, L. W. Martin, C. Hu, R. Ramesh, and S. Salahuddin, Differential voltage amplification from ferroelectric negative capacitance, *Appl. Phys. Lett.* 111, 253501 (2017).
- [6] M. Dragoman, M. Aldrigo, M. Modreanu, and D. Dragoman, Extraordinary tunability of high frequency devices using Hf<sub>0.3</sub>Zr<sub>0.7</sub>O<sub>2</sub> ferroelectric at very low applied voltages, *Appl. Phys. Lett.* 110, 103104 (2017).
- [7] M. Dragoman, M. Modreanu, I. M. Povey, S. Iordanescu, M. Aldrigo, C. Romanitan, D. Vasilache, A. Dinescu, and D. Dragoman, Very large phase shift of microwave signals in a Hf<sub>x</sub>Zr<sub>1-x</sub>O<sub>2</sub> ferroelectric at ±3V, *Nanotechnology* 28, 38LT04 (2017).
- [8] M. Dragoman, M. Modreanu, I. Povey, S. Iordanescu, M. Aldrigo, A. Dinescu, D. Vasilache, C. Romanitan, 2.55 GHz miniaturised phased antenna array based on 7 nm-thick Hf<sub>x</sub>Zr<sub>1-x</sub>O<sub>2</sub> ferroelectrics, *Electronics Letters* (2018), doi: 10.1049/el.2018.0111.
- [9] V. Garcia and M. Bibes, Ferroelectric tunnel junctions for information storage and processing, *Nature Commun.* 5, 4289 (2014).

1  
2  
3 [10] E. W. Cowell III, N. Alimardani, C. C. Knutson, J. F. Conley Jr., D. A. Keszler, B. J.  
4 Gibbons, and J. F. Wager, Advancing MIM electronics: amorphous metal electrodes, *Advanced*  
5 *Materials* 23, 74-78 (2011).  
6  
7

8  
9 [11] A. Chanthbouala, A. Crassous, V. Garcia, K. Bouzehouane, S. Fusil, X. Moya, J. Allibe, B.  
10 Dlubak, J. Grollier, S. Xavier, C. Deranlot, A. Moshar, R. Proksch, N. D. Mathur, M. Bibes, and  
11 A. Barthelemy, Solid-state memories based on ferroelectric tunnel junctions, *Nature*  
12 *Nanotechnology* 7, 101-104 (2012).  
13  
14  
15

16  
17 [12] W. J. Hu, Z. Wang, W. Yu, and T. Wu, Optically controlled electroresistance and  
18 electrically controlled photovoltage in ferroelectric tunnel junctions, *Nature Commun.* 7, 10808  
19 (2016).  
20  
21  
22

23  
24 [13] Z. Xi, J. Ruan, C. Li, C. Zheng, Z. Wen, J. Dai, A. Li, and D. Wu, Giant tunnelling  
25 electroresistance in metal/ferroelectric/semiconductor tunnel junctions by engineering the  
26 Schottky barrier, *Nature Commun.* 8, 15217 (2017).  
27  
28  
29

30  
31 [14] G. Moddel, S. Grover, *Rectenna Solar Cells*, Springer, New York (2013).  
32

33 [15] J. Wang, Se. S. Mottaghian, and M. F. Barough, Passivation properties of atomic-layer-  
34 deposited hafnium and aluminum oxides on Si surfaces, *IEEE Trans. Electron Dev.* 59, 342-348,  
35 2012.  
36  
37  
38

39 [16] J. C. Vandana, N. Batra, J. Panigrahi, R. Singh, K. K. Maurya, R. Srivastava, P. K. Singh,  
40 Silicon surface passivation using thin HfO<sub>2</sub> films by atomic layer deposition, *Applied Surface*  
41 *Science* 357, 635-642 (2015).  
42  
43  
44

45 [17] M. Modreanu, J. Sancho-Parramon, O. Durand, B. Servet, M. Stchakovsky, C. Eypert, C.  
46 Naudin, A. Knowles, F. Bridou, and M.-F. Ravet, Investigation of thermal annealing effects on  
47 microstructural and optical properties of HfO<sub>2</sub> thin films, *Appl. Surf. Sci.* 253, 328-334 (2006).  
48  
49  
50

51  
52 [18] **Supporting Information**  
53  
54  
55  
56  
57  
58  
59  
60

1  
2  
3 [19] A. Chernikova, M. Kozodaev, A. Markeev, D. Negrov, M. Spiridonov, S. Zarubin, O. Bak,  
4 P. Buragohain, H. Lu, E. Suvorova, A. Gruverman and A. Zenkevich, Ultrathin  $\text{Hf}_{0.5}\text{Zr}_{0.5}\text{O}_2$   
5 ferroelectric films on Si, ACS Applied Materials & Interfaces 8, 7232–7237 (2016).  
6  
7

8  
9 [20] A. Tselev, P. Yu, Y. Cao, L. R. Dedon, L. W. Martin, S. V. Kalinin and P. Maksymovych,  
10 Microwave a.c. conductivity of domain walls in ferroelectric thin films, Nature Communications  
11 7, 11630 (2016).  
12  
13

14  
15 [21] H. García, H. Castán, S. Dueñas, L. Bailón, F. Campabadal, O. Beldarrain, M. Zabala, M.  
16 Bagallo González, and J. M. Rafí, Electrical characterization of atomic-layer-deposited hafnium  
17 oxide films from hafnium tetrakis(dimethylamide) and water/ozone: Effects of growth  
18 temperature, oxygen source, and postdeposition annealing, J. Vac. Sci. Technol. A 31, 01A127  
19 (2013).  
20  
21

22  
23 [22] Y. W. Kim, Y. Roh, J.-B. Yoo, and H. Kim, Characteristics of atomic layer deposition  
24 grown  $\text{HfO}_2$  films after exposure to plasma treatments, Thin Solid Films 515, 2984–2989 (2007).  
25  
26

27  
28 [23] E. W. Lim and R. Ismail, Conduction mechanism of valence change resistive switching  
29 memory: a survey, Electronics 4, 586–613 (2015).  
30  
31

32  
33 [24] Z. Dong, X. Cao, T. Wu, and J. Guo, Tunneling current in  $\text{HfO}_2$  and  $\text{Hf}_{0.5}\text{Zr}_{0.5}\text{O}_2$ -based  
34 ferroelectric tunnel junction, J. Appl. Phys. 123, 094501 (2018).  
35  
36

37  
38 [25] S. Daskalakis, J. Kimionis, J. Hester, A. Collado, Manos M. Tentzeris, and A. Georgiadis,  
39 Inkjet printed 24 GHz rectenna on paper for millimeter wave identification and wireless power  
40 transfer applications, 2017 IEEE MTT-S International Microwave Workshop Series on  
41 Advanced Materials and Processes for RF and THz Applications (IMWS-AMP) (2017), pp. 1-3,  
42 20-22 September 2017, Pavia, Italy  
43  
44  
45

46  
47 [26] S. Hanson, M. Seok, Y.-S. Lin, Z. Y. Foo, D. Kim, Y. Lee, N. Liu, D. Sylvester, and D.  
48 Blaauw, A low-voltage processor for sensing applications with picowatt standby mode, IEEE J.  
49 Solid-State Circuits 44, 145–154 (2009).  
50  
51  
52  
53  
54  
55  
56  
57  
58  
59  
60

1  
2  
3  
4  
5  
6  
7  
8  
9  
10  
11  
12  
13  
14  
15  
16  
17  
18  
19  
20  
21  
22  
23  
24  
25  
26  
27  
28  
29  
30  
31  
32  
33  
34  
35  
36  
37  
38  
39  
40  
41  
42  
43  
44  
45  
46  
47  
48  
49  
50  
51  
52  
53  
54  
55  
56  
57  
58  
59  
60

[27] H. Jayakumar, K. Lee, W. S. Lee, A. Raha, Y. Kim, and V. Raghunathan, Powering the internet of things, Proceedings of the 2014 International Symposium on Low Power Electronics and Design, ISLPED '14, 2014. doi: 10.1145/2627369.2631644.

**Figure captions**

Fig. 1 (a) Surface morphology and phase image (b) of the  $\text{Hf}_{0.45}\text{Zr}_{0.55}\text{O}_{1.76}$  thin film obtained by applying sequentially a bias of +2/-2 V during the scan. The bright stripes in (b) were obtained with +2 V and the dark stripes with -2 V; (c) Optical image of top electrodes of  $\text{Hf}_{0.45}\text{Zr}_{0.55}\text{O}_{1.76}$  capacitors, and (d) schematic of the cross-section of the MFS device.

Fig. 2 C-V dependence of the MFS device at 100 kHz, for different sweeping ranges. Inset: Dependence of the windows of C-V curves on the sweeping range.

Fig. 3 (a) DC I-V dependence of the MFS device. Top inset: Fitting of I-V data with Fowler-Nordheim tunneling mechanism. Bottom inset: I-V dependence in a semi-log representation, with the same line style. (b) Band diagrams for the ON and OFF states in the absence of an applied bias

Fig. 4 Optical image of the antenna array at 26 GHz.

Fig. 5 (a) Return loss  $|S_{11}|$  of the antenna array, and (b) imaginary part of its input impedance.

Fig. 6 Circuit layout of the harvester.

Fig. 7 Time domain response of the harvester.

Fig. 8 Predicted responsivity and NEP of the harvester at 26 GHz for different input powers.

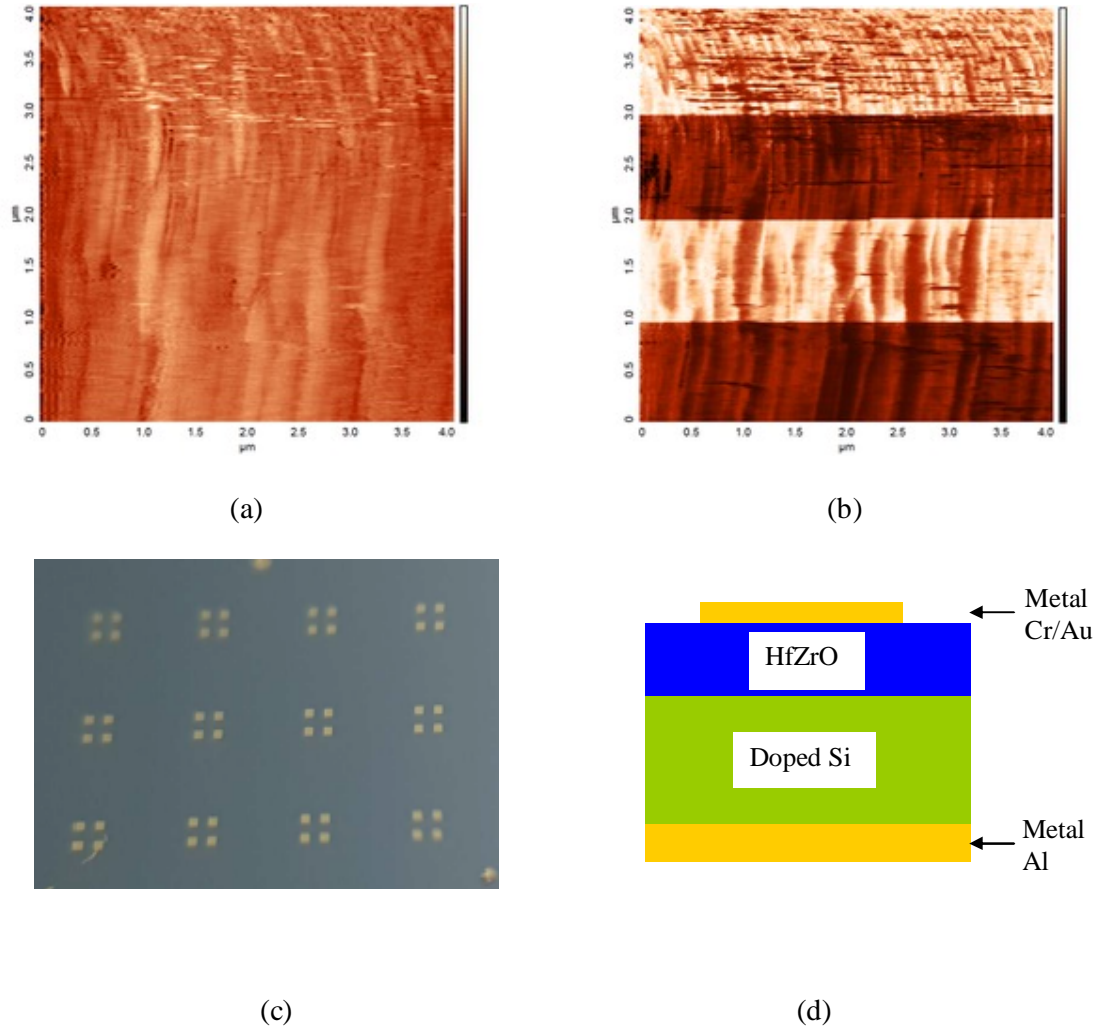


Fig. 1

1  
2  
3  
4  
5  
6  
7  
8  
9  
10  
11  
12  
13  
14  
15  
16  
17  
18  
19  
20  
21  
22  
23  
24  
25  
26  
27  
28  
29  
30  
31  
32  
33  
34  
35  
36  
37  
38  
39  
40  
41  
42  
43  
44  
45  
46  
47  
48  
49  
50  
51  
52  
53  
54  
55  
56  
57  
58  
59  
60



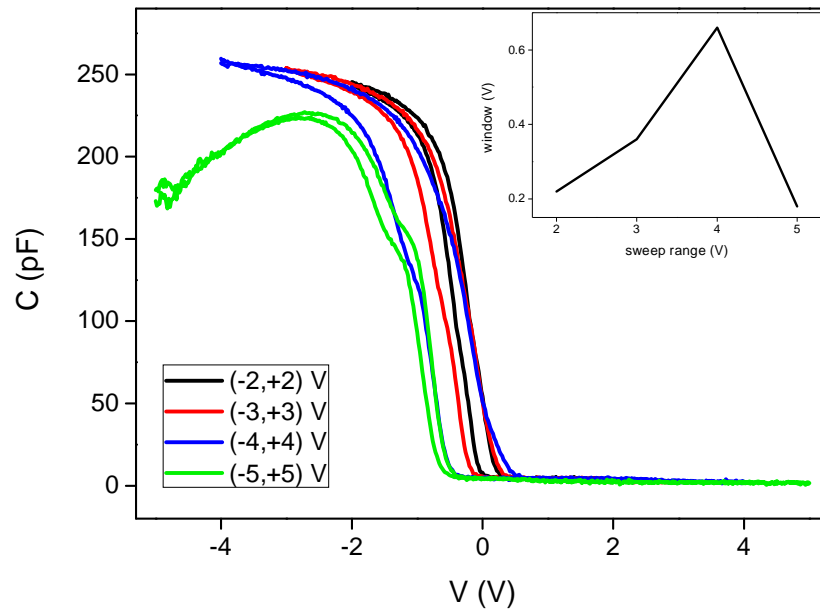
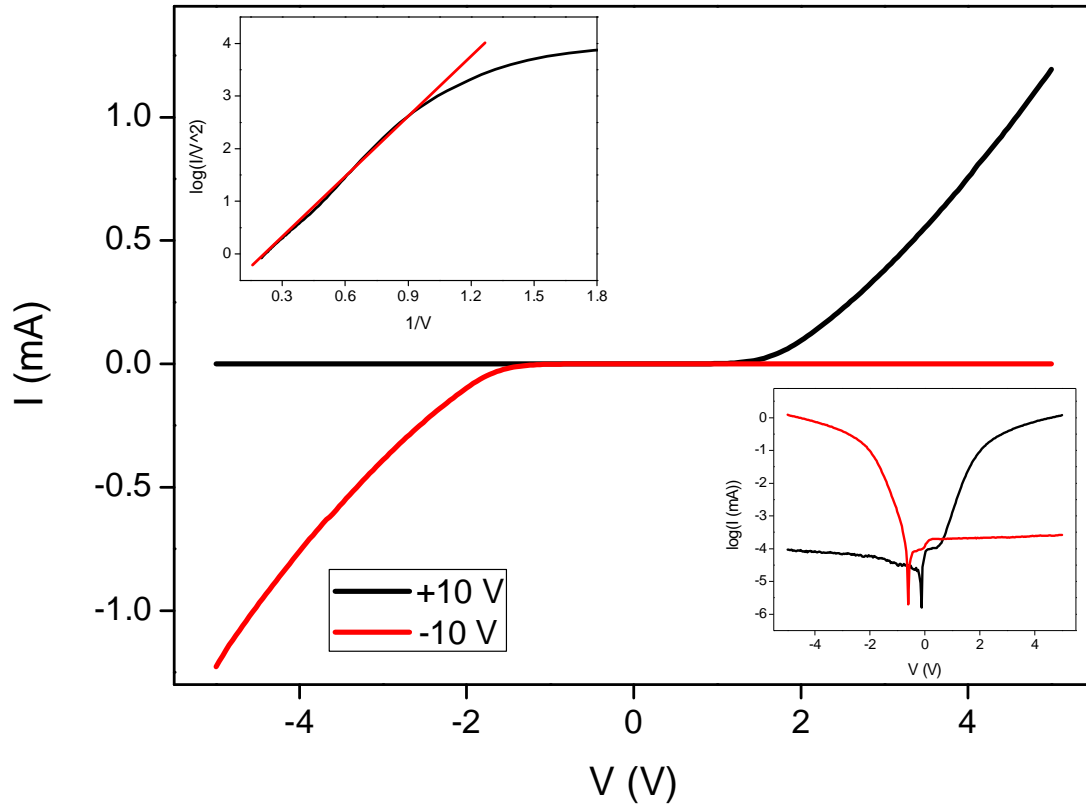
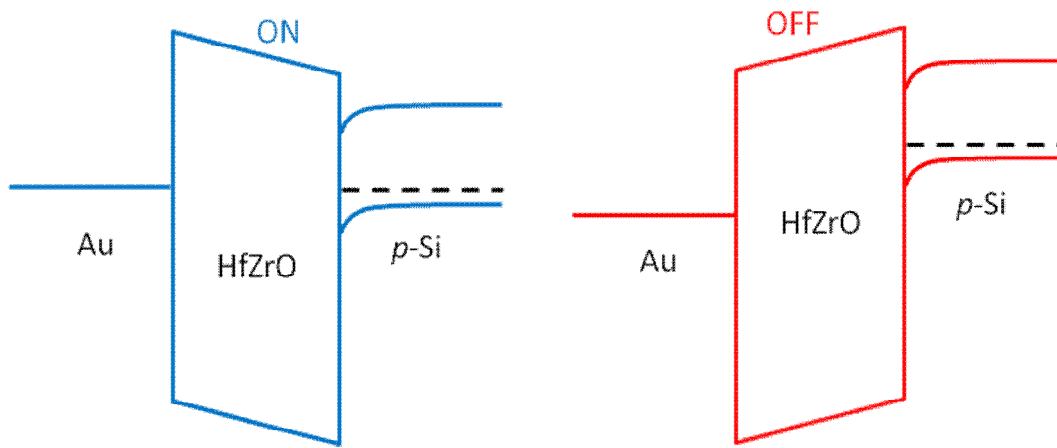


Fig. 2



(a)



(b)

Fig. 3

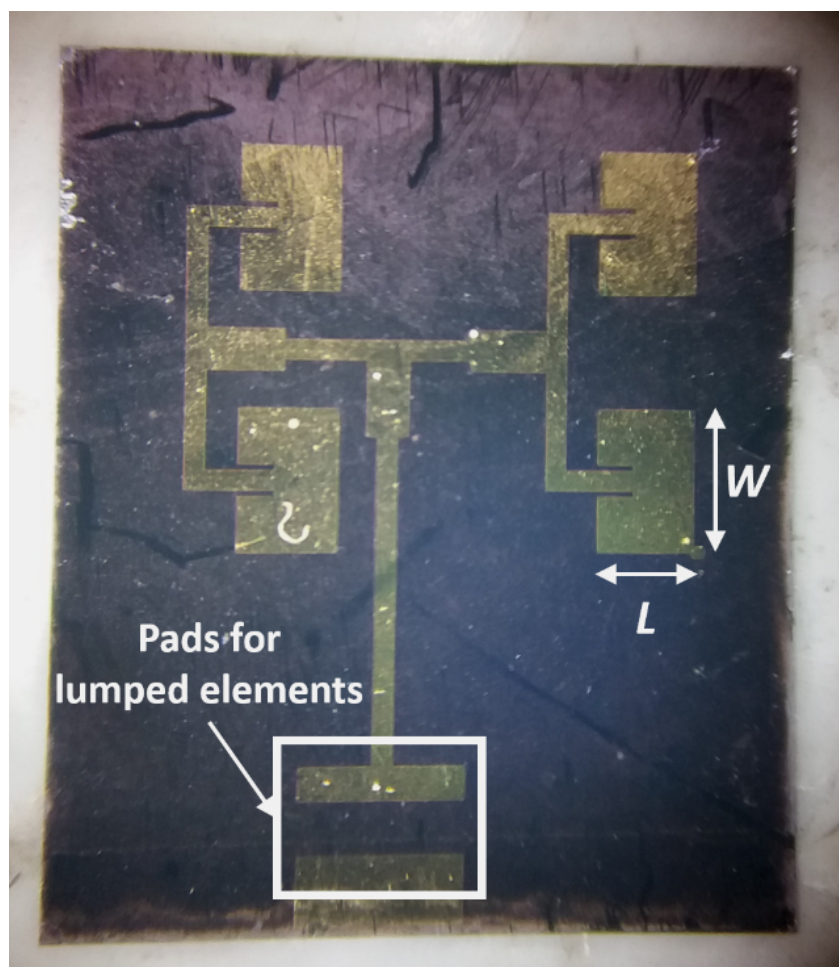
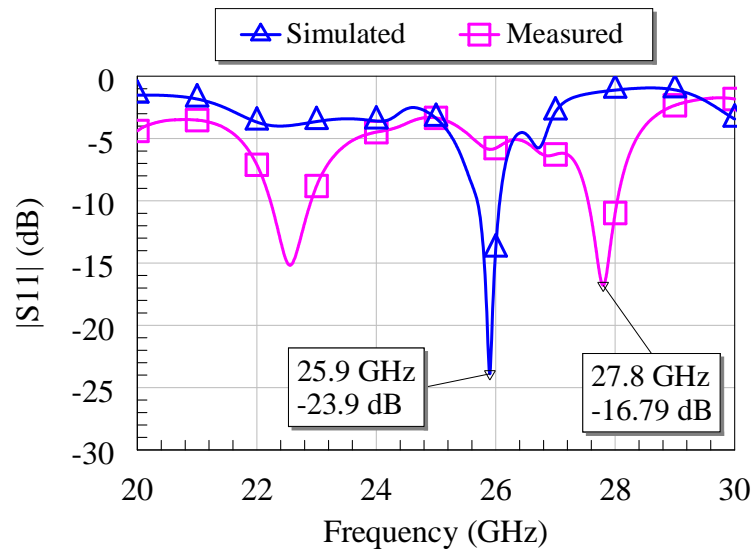
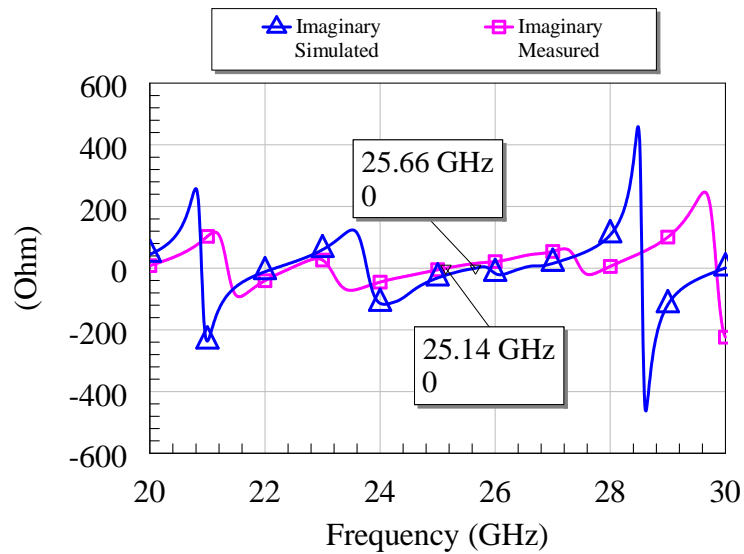


Fig. 4



(a)



(b)

Fig. 5

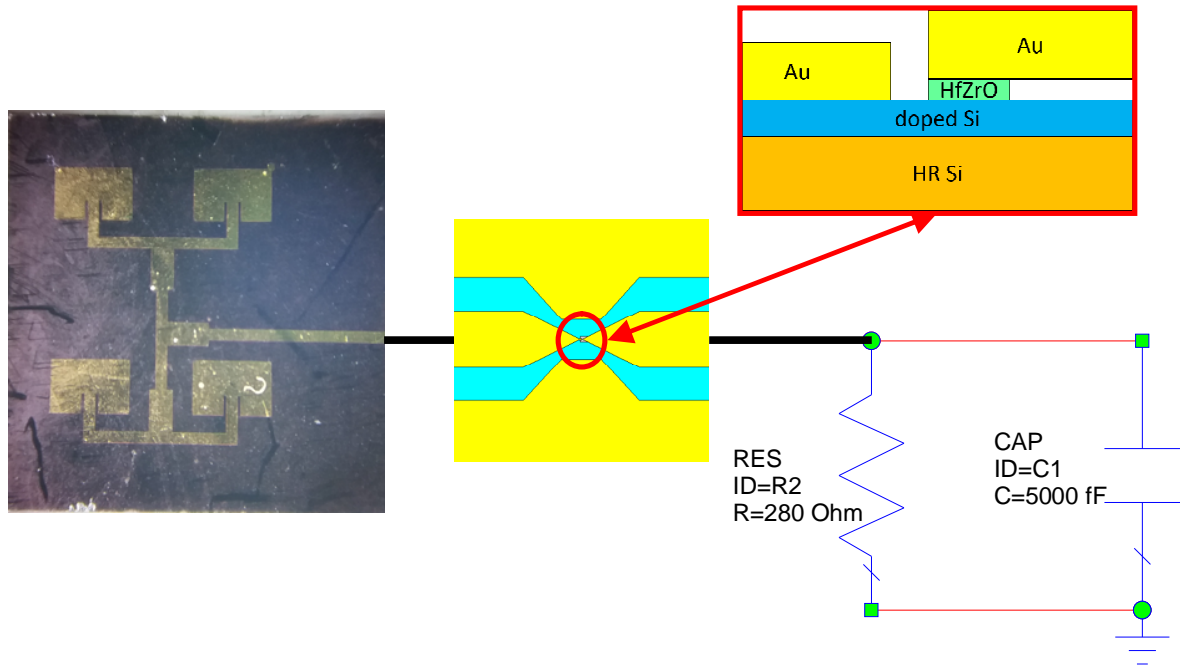


Fig. 6

1  
2  
3  
4  
5  
6  
7  
8  
9  
10  
11  
12  
13  
14  
15  
16  
17  
18  
19  
20  
21  
22  
23  
24  
25  
26  
27  
28  
29  
30  
31  
32  
33  
34  
35  
36  
37  
38  
39  
40  
41  
42  
43  
44  
45  
46  
47  
48  
49  
50  
51  
52  
53  
54  
55  
56  
57  
58  
59  
60

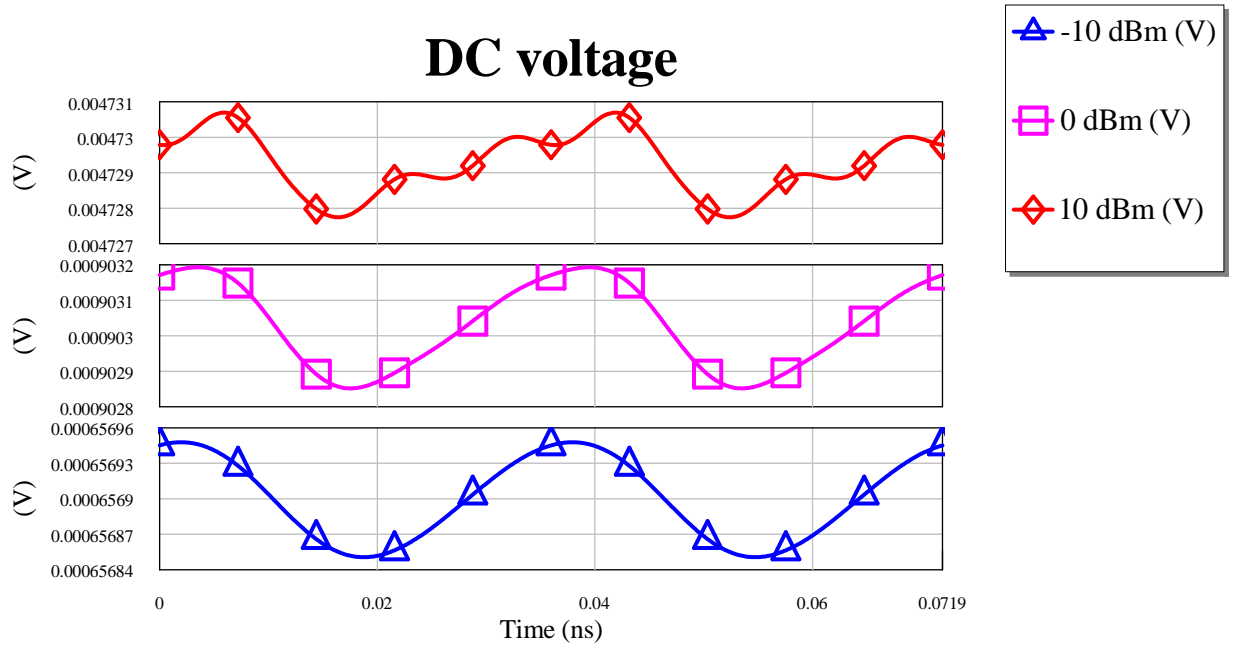


Fig. 7

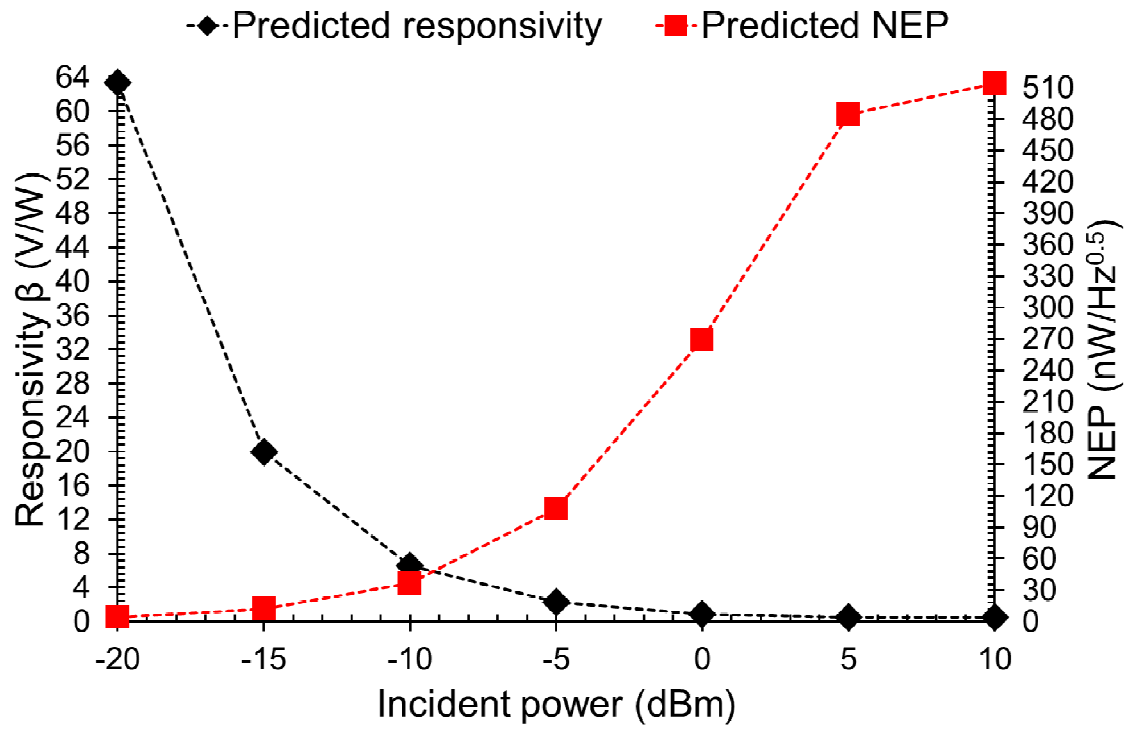


Fig. 8